APPENDIX 1

"Fitting Flux Ropes to a Global MHD solution: A comparison of techniques"

Pete Riley, J. A. Linker, R. Lionello, Z. Mikic, D. Odstrcil, M. A. Hidalgo, C. Cid, Q. Hu, R. P. Lepping, B. J. Lynch, and A. Rees

Accepted for publication in the *Journal of Atmospheric and Solar Terrestrial Physics*, 2004.

Fitting Flux Ropes to a Global MHD solution: A comparison of techniques

Pete Riley, J. A. Linker, R. Lionello, and Z. Mikić

Science Applications International Corporation, San Diego. CA 92121, USA

D. Odstrcil

Center for Integrated Research in Environmental Sciences, University of Colorado and Space Environment Center, National Oceanic and Atmospheric Administration, Boulder, CO 80305, USA

M. A. Hidalgo, C. Cid

Departamento de Fisica, Universidad de Alcalá, Alcalá de Henares, Madrid, Spain

Q. Hu *

Bartol Research Institute, University of Delaware, Newark, DE, USA

R. P. Lepping

Laboratory for Extraterrestrial Physics, NASA-Goddard Space Flight Center, Greenbelt, MD 20771, USA

B. J. Lynch

Department of Atmospheric, Oceanic, and Space Sciences, University of Michigan, Ann Arbor, Michigan, USA

A. Rees

The Blackett Laboratory, Imperial College London, London SW7 2BW UK

Abstract

Flux rope fitting (FRF) techniques are an invaluable tool for extracting information about the properties of a sub-class of CMEs in the solar wind. However, it has proven difficult to assess their accuracy since the underlying global structure of the CME cannot be independently determined from the data. In contrast, large-scale MHD simulations of CME evolution can provide both a global view as well as localized time series at specific points in space. In this study we apply 5 different

fitting techniques to 2 hypothetical time series derived from MHD simulation results. Independent teams performed the analysis of the events in "blind tests", for which no information, other than the time series, was provided. From the results, we infer the following: (1) Accuracy decreases markedly with increasingly glancing encounters; (2) Correct identification of the boundaries of the flux rope can be a significant limiter; and (3) Results from techniques that infer global morphology must be viewed with caution. In spite of these limitations, FRF techniques remain a useful tool for describing in situ observations of flux rope CMEs.

Key words: coronal mass ejection, magnetic cloud, magnetic flux rope, magnetohydrodynamic simulation, solar wind, Sun, heliosphere

1 Introduction

Coronal Mass Ejections (CMEs) are undoubtedly one of the most impressive forms of transient solar activity. In addition to expelling huge amounts of solar material (10^{15-16} grams) into interplanetary space (Hundhausen, 1987), a large energy budget (10^{31-32} ergs) is needed, which presumably is supplied by the magnetic field. CMEs appear to play a fundamental role in the way the corona responds to changes in the solar magnetic field by providing a mechanism for the Sun to shed magnetic flux (which is thought to be essential to the cyclic renewal of the solar dynamo). They also contribute a small but significant amount to the overall solar wind flow at low latitudes; perhaps as much as 15% of the average mass flux in the low-latitude solar wind during solar maximum (Webb and Howard, 1994). CMEs, and particularly fast CMEs, have been identified as the leading cause of non-recurrent geomagnetic storms and they can also enhance the geo-effectiveness of recurrent storms (Gosling, 1990).

The interplanetary CMEs that concern us in this study have clear, coherent magnetic characteristics. We will call them flux ropes, acknowledging that, for the most part, they conform to the three defining characteristics of a Magnetic Cloud (MC): (1) A strong magnetic field; (2) a large rotation in the field; and (3) a low proton temperature (Burlaga et al., 1981).

Using models to interpret in situ measurements can provide important insight into the global properties of both flux rope and non-flux rope CMEs. In addition, models that include dynamic effects allow us to model the eruption and evolution of CMEs conveniently and through regions of space not currently accessible by spacecraft. The models span a broad spectrum of sophistication

* now at IGPP University of California, Riverside, USA

as they attempt to address different aspects of interplanetary CME structure and evolution. Flux rope fitting (FRF) models have been applied to in situ data for more than 20 years. Beginning with linear force-free models (Goldstein, 1983; Lepping et al., 1990), they have evolved to include the effects of expansion (Osherovich et al., 1993; Marubashi, 1997), data from multiple spacecraft (Mulligan et al., 2001), non-force free effects (Mulligan et al., 2001; Hidalgo et al., 2002), elliptical geometries (Hidalgo, 2003), the development of a Grad-Shafranov reconstruction technique (Hu and Sonnerup, 2001, 2002), and the generalization of the Lundquist solution for an oblate cylinder (Vandas and Romashets, 2003). In contrast, sophisticated global MHD models have recently been developed to study the initiation and evolution of flux rope CMEs all the way from the Sun to 5 AU (e.g., Riley et al. (2003)).

An unresolved issue with FRF models has been that there is no independent way to assess the errors of the fit. One can, and does of course, compute deviations from the observed data with the derived profiles. In fact, minimizing this deviation defines the best fit to the data. Lepping et al. (2003), for example, performed a detailed study on estimated errors in magnetic cloud model fit parameters by adding noise to known solutions. They found $1-\sigma$ uncertainties in the orientations of the flux rope axes of $20-30°$ and ± 0.3 in the value of the impact parameter. Yet even a "reasonable" fit does not guarantee that the derived parameters are "correct". To do so would require knowledge of the global properties of the event, parameters that cannot be determined independently. On the other hand, global MHD solutions can provide both the global structure of the event as well as localized point measurements.

The purpose of this study is to assess 5 fitting models using hypothetical time series created with an MHD solution. We begin by describing the MHD model. Following this, each fitting techniques is described. These are representative of the spectrum of approaches that are employed today to obtain flux rope parameters. We then summarize the results from each team and compare a subset of inferred parameters that were computed by every team, specifically, the orientation of the flux rope axis and the distance of closest approach. Finally, we summarize the main results from this study, discuss its implications, and suggest what still remains to be done.

It is important to stress that our goal is not to rank the various fitting techniques. In fact we will show that there are distinct advantages and disadvantages associated with each. Rather we conclude that it is *how* the technique is applied, rather than *which* technique is applied, that impacts the results of the fit most significantly.

2 The Models

2.1 Global MHD Model

A description of the solar and heliospheric MHD models used to generate the results presented here has been provided elsewhere (Odstrcil et al., 2002). It has previously been applied to: (1) Interpreting the global context of a CME observed by two spacecraft (Riley et al., 2003); (2) studying post-eruption reconnection associated with CMEs in the solar wind (Riley et al., 2002b); (3) distortion of a CME and shape of the shock (Odstrcil et al., 2002); and (4) generation of synthetic white-light heliospheric images (Odstrcil et al., ????). Here we will confine ourselves to a few comments pertinent to the present study. We have simulated the eruption, propagation, and evolution of a generic CME all the way from the solar surface to 1 AU. Two models are coupled together to achieve this. Between the solar surface (1 R_S) and 30 R_S we use SAIC's coronal MHD model (Mikić and Linker, 1994). From $30R_S$ to 5 AU we use CU/CIRES-NOAA/SEC's heliospheric MHD model (Odstrcil and Pizzo, 1999). Output from the outer boundary of the coronal model is used directly as the inner boundary conditions for the heliospheric model. Splitting the modeling region into two like this is computationally more efficient (as the heliospheric code is allowed to run at much larger time steps), and, moreover, takes advantage of the expertise built into each code in simulating that particular environment.

The models contain a number of approximations, which have been discussed in detail by Riley et al. (2003). However, for the purposes of generating hypothetical time series, the main concern is that the time series bear a reasonable resemblance to observed magnetic clouds. We have shown (Riley et al., 2002b, 2003) that while the simulations do not mimic any one event in detail, they do provide a good generic approximation to fast CMEs observed in the solar wind, particularly with regard to their magnetic characteristics.

2.2 Force-Free Models

Three of the fitting techniques employed in this study fall under the general classification of linear force-free models, and share the following basic features. First and foremost is the assumption that the magnetic cloud under consideration can be approximated by a force-free configuration. Based on a suggestion by Goldstein (1983), Burlaga (1988) developed the idea that magnetic clouds in the solar wind could be approximated by a constant-α, force-free, cylindrically-symmetric configuration, or in other words, the Lundquist (1950)

solution. Expressed in cylindrical coordinates aligned with the flux rope, the solution describes a set of helical field lines, which, as one moves away from the axis increase in twist. Thus the axial field line is straight, while the field line at the boundary of the cloud is circular. Fitting this solution to in situ measurements is accomplished in two steps. In the first step, a χ^2 minimization procedure is performed on the magnetic field components to yield the orientation of the flux rope and the impact parameter (i.e., the closest distance to the axis reached by the spacecraft). In the second step, a χ^2 minimization procedure is performed on the magnetic field magnitude to determine the axial field strength. In some methods, minimum variance (Sonnerup and Cahill, 1967) is applied to initially localize the orientation of the flux rope (Lepping et al., 1990), with the intermediate variance direction tending to align itself with the axis of the cloud. It has been shown, however, this approach becomes increasingly inaccurate as the spacecraft passes further from the cloud axis. Lepping et al. (1990) estimated that for encounters that pass only to within 60% of the cloud axis, the error in the calculated angle was of the order of 10°. By 90% this increases to $\sim$ 20°. A notable difference between this (and the other fitting) techniques and the MHD model is that whereas the former assume straight cyclinders, the MHD model assumes a toroidal geometry. It is unlikely, however, that this difference would affect the results of this study in any significant way.

2.3 Elliptical Cross-Section Model

Hidalgo et al. (2002) relaxed the assumption that the flux rope has to be force free by relating the magnetic field vectors to the current density of the cloud. Drawing on early work by Chen (1996), who derived the magnetic field within a flux rope near the Sun in terms of the currents within it, they used Maxwell's equations for the magnetic field to relate the poloidal (toroidal) component of the magnetic field to the toroidal (poloidal) component of the current density. There are several practical benefits from such an approach: (1) The number of free parameters is reduced from 7 to 5; (2) There is no need to use minimum variance to initially determine the orientation of the flux rope axis so that the fitting procedure occurs in one step; and (3) In addition to the standard parameters, a measure of the current density within the magnetic cloud can be estimated. The finite amplitude of the current density perpendicular to the flux rope led them to conclude that potentially significant pressure gradients exist within the clouds that are not incorporated in the force-free approximation.

Hidalgo et al. (2002) generalized their technique to include elliptical cross sections, the logic being that interaction with the ambient solar wind would lead to a deformation of the initially cylindrically shaped flux rope. To accomplish this, they solved Maxwell's equations for the magnetic field and the plasma

continuity equation in elliptical coordinates. This produced a parameter η that is associated with the eccentricity of the cross-section of the flux rope. Most recently, Hidalgo (2003) further generalized their technique to incorporate the expansion of the flux rope as it propagates through the interplanetary medium. It is this version of the technique that is employed in this study.

2.4 Grad-Shafranov Reconstruction Technique

Initially developed for studies of the magnetopause (Sonnerup and Guo, 1996; Hau and Sonnerup, 1999; Hu and Sonnerup, 2000), and subsequently applied to flux rope observations (Hu and Sonnerup, 2001, 2002; Hu et al., 2003), the Grad-Shafranov Reconstruction (GSR) technique makes two basic assumptions: (1) that the structure under consideration is in approximate magnetostatic equilibium; and (2) that is cylindrical, i.e., 2.5D in a Cartesian coordinate. From this, it follows that the global asymmetric structure of the cloud perpendicular to its axis can be recovered. It should be noted that the orientation of the flux rope's axis is calculated mainly based on the Grad-Shafranov equation. It is also noteworthy that the boundaries of the cloud need not first be identified in the data. They are, in fact, an output of the model (Hu et al., 2003).

3 Results

3.1 The MHD Solution

Although the teams were not informed, we chose to construct the two test cases from the same simulation by positioning a hypothetical spacecraft at two different locations. An axisymmetric (2.5-D) solution was used for simplicity. Thus the parameters derived for each (with the exception of the distance of closest approach) should be the same. Figure 1 shows a cross section of the flux rope as it approaches 1 AU. The heliospheric portion of the simulation spans $\pm 60°$ in latitude. The flux rope is indicated by the closed meridional field lines (black lines) and shows significant distortion. Most of this is due to kinematic effects as the initially circular CME expands into the spherical geometry of the solar wind (Riley and Crooker, 2004). Other aspects of this simulation have been discussed by Riley et al. (2002a) and Riley et al. (2003). Since the cloud is axisymmetric, it is self-evident that the latitudinal and longitudinal orientations of the axis are: $\Lambda = 0°$, and $\varphi = -90°$, respectively. From the direction of the magnetic field vectors, it is straightforward to show that the sign of the helicity is -1 (or left-handed).

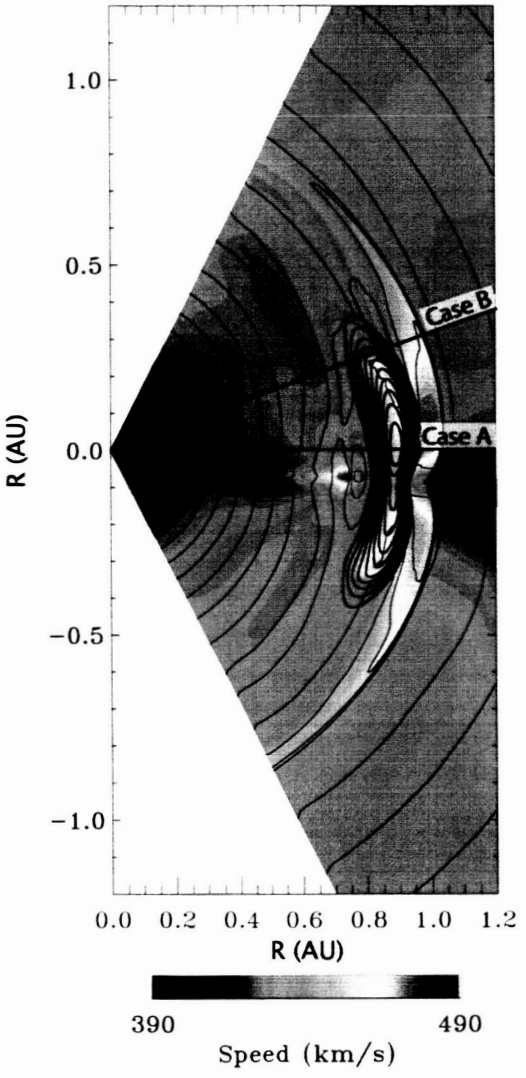

Fig. 1. Meridional cross section of evolving flux rope as it approaches 1 AU. The simulation domain extends ±60° in latitude. The contours denote radial velocity (color); density (red lines); and magnetic field (black lines). The straight lines labeled 'Case A' and 'Case B' indicate the latitude at which the simulated time series were taken.

The two straight lines labeled 'Case A' and 'Case B' show the latitude from which the two test cases were constructed. We clarify that the time series were not made by flying along these lines toward the Sun, but were recorded at 1 AU as the disturbance passed over that point. For case A, the spacecraft was located at a latitude, $\Lambda = 0$, at 1 AU, and flies effectively through the center of the flux rope. In fact, the CME was launched 10° below the equator, but the effect of the plasma sheet has caused it to become compressed locally, effectively displacing the center of the axis of the flux rope to the equator. For the purposes of this study, any computed impact parameter (P, the distance of closest approach) ≤ 0.1 should be considered consistent with the MHD results. As illustrated in Figure 1, case B represents a "glancing" encounter at

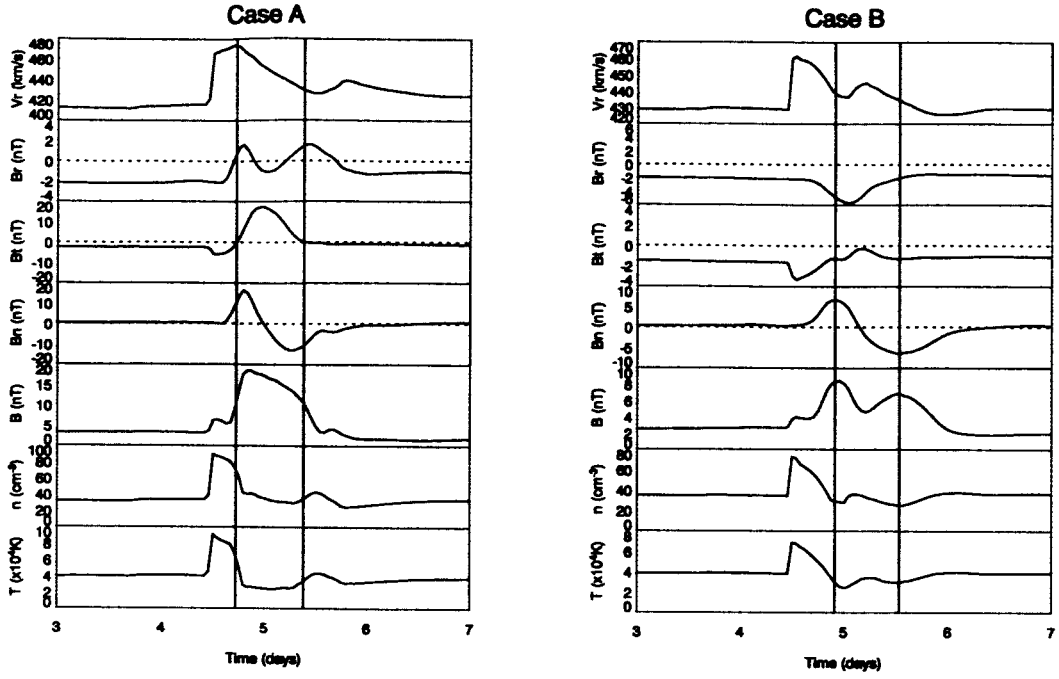

Fig. 2. Hypothetical time series constructed by positioning a spacecraft at the two latitudes shown in Figure 1 at 1 AU. Both panels show from top to bottom: Radial velocity (vr); the 3 components of the magnetic field (Br, Bt, Bn); the magnetic field magnitude (B); the plasma number density (n); and the plasma temperature (T). The panels on the left summarize case A, while the panels on the right summarize case B. The vertical lines mark the boundary of the flux rope.

$18.0°N$ latitude. The northern edge of the FR was located at $25.8°N$, so that the impact parameter, P, for case B is estimated to be $\sim 18.0/25.8 = 0.7$.

The time series generated from hypothetical spacecraft positioned at the latitudes indicated in Figure 1 are shown in Figure 2. Focusing first on case A, the plasma and magnetic field parameters show the classic signatures of a fast flux rope CME. In particular: The declining speed profile, indicating expansion of the ejecta; a fast forward shock ahead of, and being driven by, the ejecta; density and temperature depressions; clear, coherent rotations in the magnetic field; an asymmetric enhancement in the magnetic field strength. Similar, although less pronounced, features can be discerned in the profiles of case B. Note, however, that the magnetic field magnitude profile is inverted; instead of rising to a peak and declining the field strength decreases to a minimum and then rises.

The data shown in Figure 2 were given to each team. Data at two resolutions (1 minute and 1 hour) were requested. Since the scale size of CME and its associated disturbance is significantly longer than 1 hour, no significant information was lost by analyzing the 1 hour data set. The teams were not provided with any other information, in particular, they were not given the location of the boundaries.

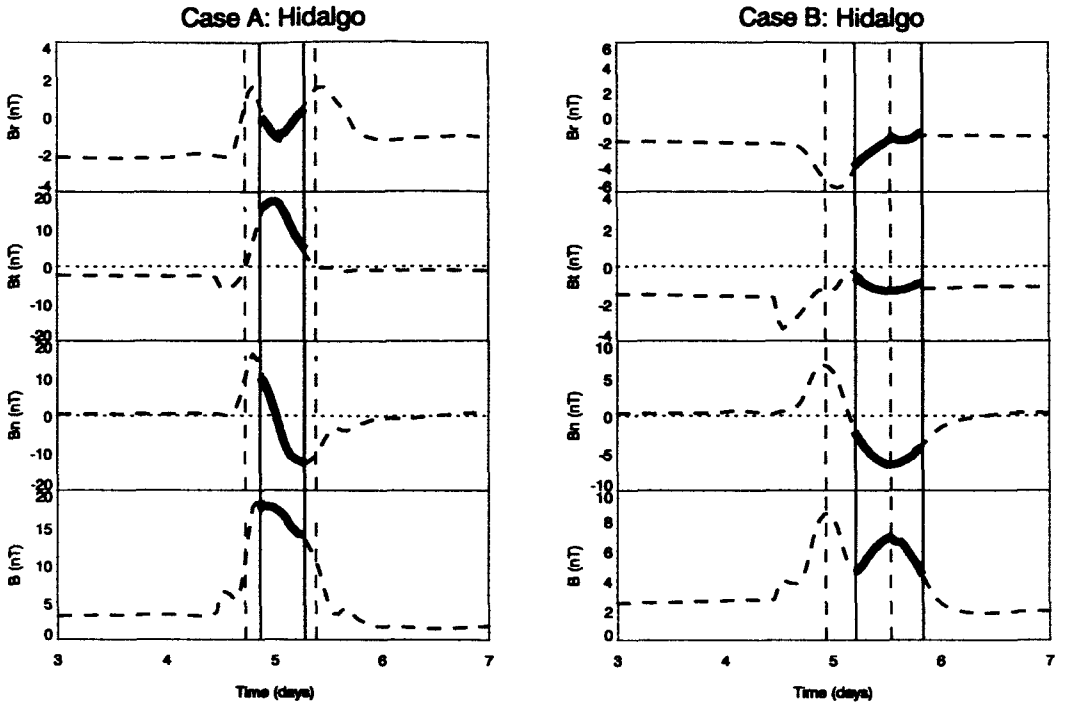

Fig. 3. A subset of the data shown in Figure 2. Both panels show from top to bottom: 3 components of the magnetic field (Br, Bt, Bn), and the magnetic field magnitude (B). Overlaid on each are the results from the Elliptical cross-section model. The solid vertical lines mark the boundary of the flux rope as determined by team 1, while the dashed lines mark the MHD boundaries of the flux rope.

In the following sections we summarize the fits individually, focusing on how well each approach reproduced the MHD time series. Following this, we summarize and compare some of the fitted parameters.

3.2 Team 1 (Elliptical Cross-Section Model)

The first team, led by M. A. Hidalgo, applied the elliptical cross-section model to the simulated time series. Their fits are compared with the MHD results in Figure 3. The fits in both cases are exceptionally good. In case A, the boundaries chosen for the elliptical cross-section model fall within the MHD boundaries, however, they appear to have captured the essential elements of the flux rope. In contrast, for case B, the region identified as "flux rope" in fact only encompasses the trailing edge of the flux rope. In spite of this, the fit mimics the MHD profiles very well. The elliptical cross section model, not surpisingly, provides an estimate of the ellipticity of the flux rope. For both cases, values of 0.56 were obtained. While these values underestimate the true ellipticity (See Figure 1), they deviate significantly from the circular cross sections assumed in the force-free models.

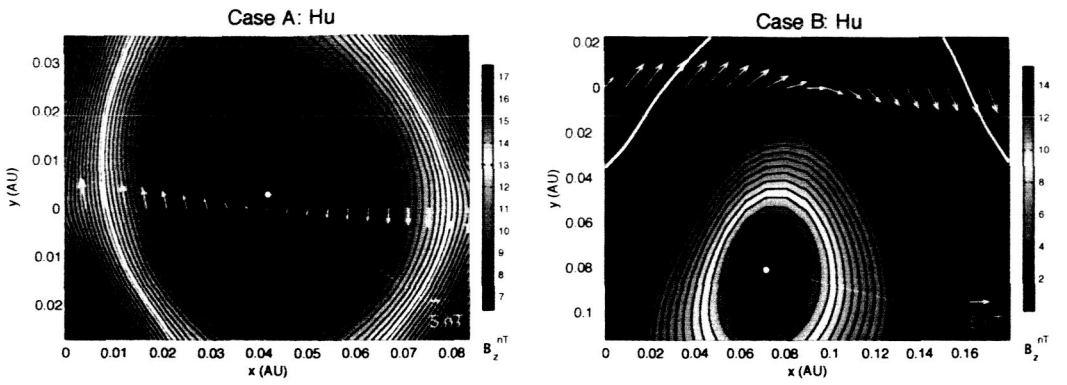

Fig. 4. Recovered cross sections for case A (left) and case B (right). Black contour lines are transverse magnetic field lines on the x-y plane. Overlaid colors are the component, Bz(x, y), distribution as indicated by the color bar. Arrows along y=0 are spacecraft observation of the transverse magnetic field vectors. The boundary of the flux rope is marked by the thick white curve.

3.3 Team 2 (The Grad-Shafranov Reconstruction Technique)

The second team, led by Q. Hu, applied the Grad-Shafranov Reconstruction Technique to cases A and B. The results are summarized in Figure 4. This is the only method that yields an exact fit of the observational data along the spacecraft path, since those data are utilized as spatial initial input into their model to derive the extended field of view. In addition to the three components of the magnetic field, the current density distribution can also be obtained. For this study, we focus on the global morphology aspect of the GSR technique, which is the new facet of this approach. The black contour lines show the recovered transverse component of the field. The observed magnetic field vectors are plotted along the spacecraft path (y=0). The inferred boundaries of the flux rope are shown by the solid white lines. Comparison with Figure 1 suggests that the global morphology of the CME has not been accurately recovered (note that the sun is to the right). Moreover, the cloud shape and orientation of the major axis are different in the two cases (see also, Table 1 and 2).

3.4 Team 3 (Force Free Model)

Our third team, led by R. P. Lepping, applied their linear force-free model to the simulated time series in Figure 2. Figure 5 compares these results with the MHD profiles. The fits to case A are relatively good. In addition, the boundaries chosen match the MHD boundaries very closely. Notable differences include: (1) the asymmetry in the MHD profiles that are not reproduced by the symmetric force free solution; and (2) the underestimate of B_n at the leading

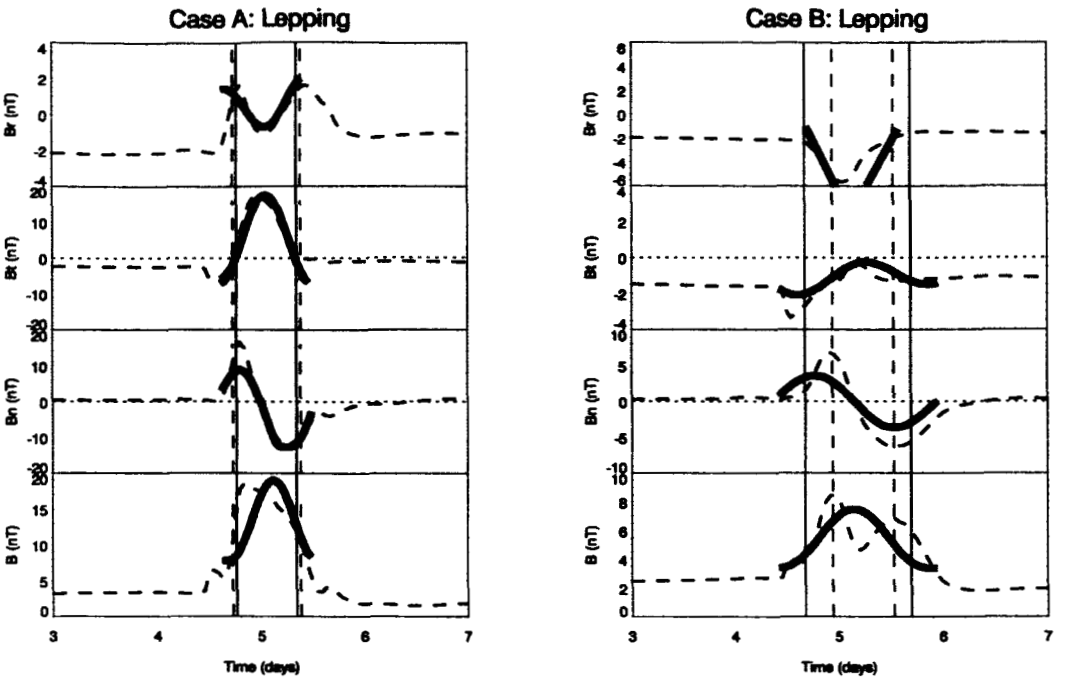

Fig. 5. As Figure 3 but for the Lepping Force Free model.

edge of the flux rope. As expected, the fits to case B are not as good. While there is a passing resemblence to the fit profiles for the individual components, the field strength does not match well. Moreover, the fitted boundaries differ significantly from the MHD boundaries: In addition to including the flux rope, they also encompass material ahead of, and behind it.

3.5 Team 4 (Force Free Model)

The fourth team, led by B. J. Lynch, also applied a similar linear force-free model. The fits to the simulated time series are shown in Figure 6. The fitted profiles for case A are very similar to the team 3 results and match the MHD profiles well. This is not surprising as the techniques employed are effectively the same. The profiles for case B, however, are markedly different. This difference stems from the choice of boundaries. In this case, the fitted boundaries fall within the ejecta but under sample it. Again, since the force free model forces a profile that includes a maximum in the field midway through, there is little hope of reproducing the MHD results.

3.6 Team 5 (Force Free Model)

The fifth and final team, led by A. Rees, again applied a similar linear force-free model to the two hypothetical CMEs. Figure 7 summarizes these fits. Once

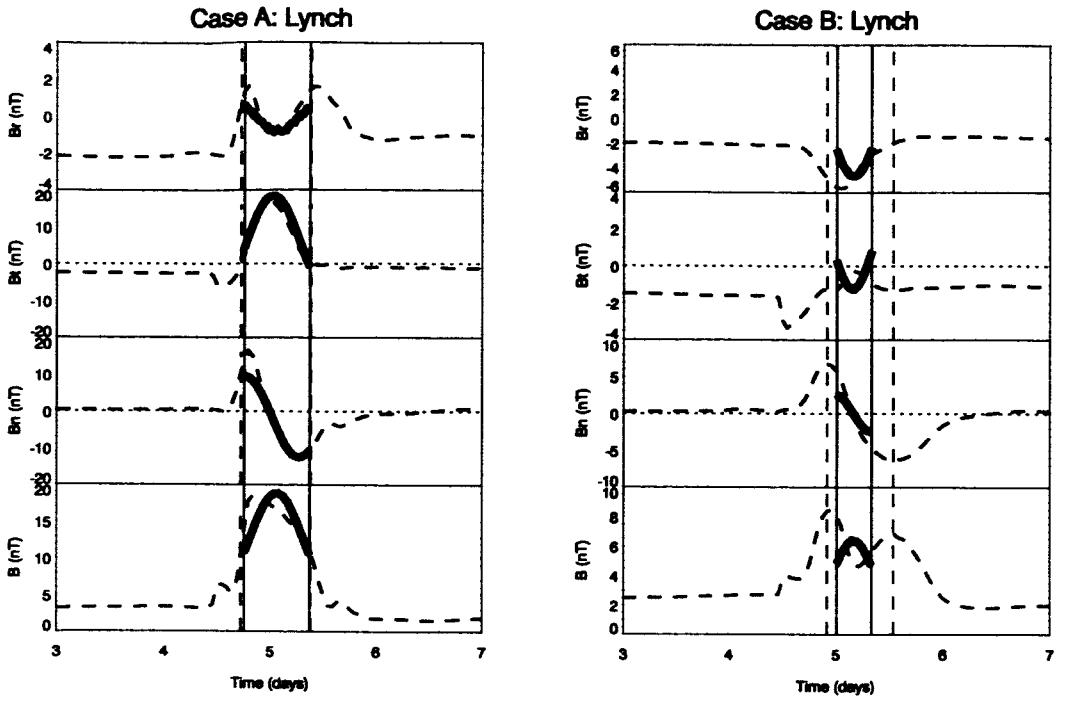

Fig. 6. As Figure 3 but for the Lynch Force Free model.

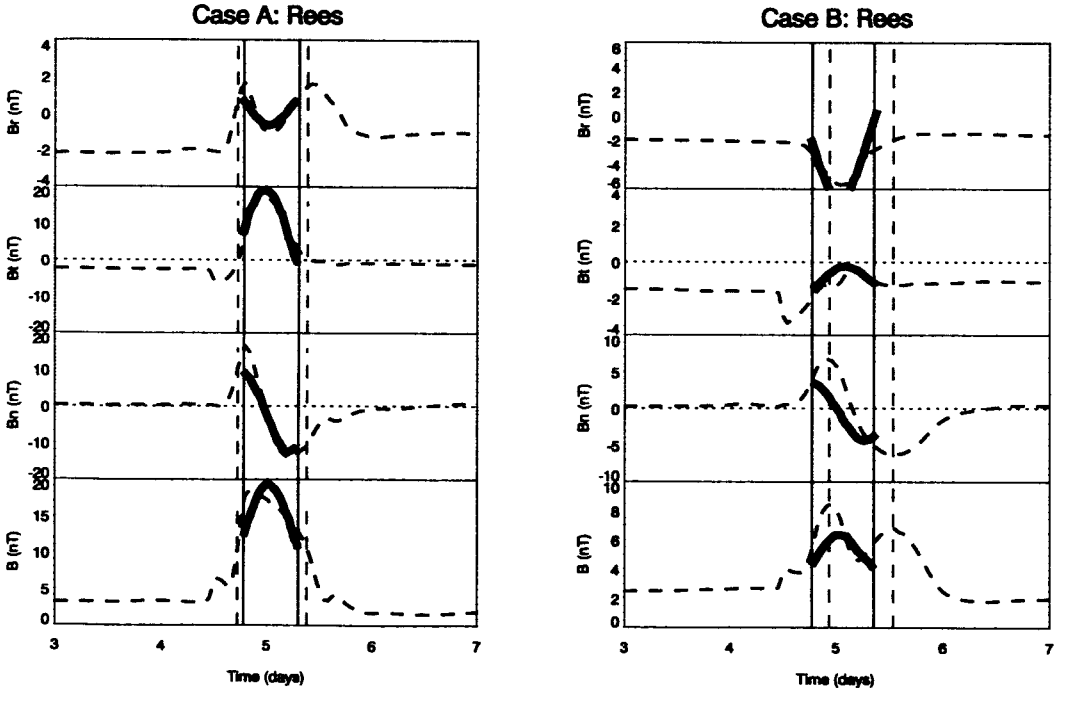

Fig. 7. As Figure 3 but for the Rees Force Free model.

again, case A is fairly well reproduced using the linear force-free approximation. Case B suffers from the same types of problems that were encountered by the other teams. This time, the boundaries were chosen in an attempt to include the first major peak in the field magnitude.

Table 1. Flux rope fit results for case A.

team	Model	$\Lambda(°)$	$\varphi(°)$	P
Riley	MHD	0	-90	< 0.1
Hidalgo	Elliptical Cross-Section	9	-85.0	0.16
Hu	GSR	15	-84.6	0.0083
Lepping-1	Linear force free	-31.5	-77.3	0.136
Lepping-2	Linear force free	-2.6	-80.1	0
Lynch-1	Linear force free	-14.3	-81.9	0.08
Lynch-2	Linear force free	-27	-80.4	0.11
Lynch-3	Linear force free	14.3	-89.2	0.00
Rees	Linear force free	10.4	-81.2	0.1

Table 2. FRF results for case B.

team	Model	$\Lambda(°)$	$\varphi(°)$	P
Riley	MHD	0	-90	0.7
Hidalgo	Elliptical Cross-Section	-11	-165	—
Hu	GSR	-4.0	-65.1	0.54
Lepping	Linear force free	2.8	-31.5	0.401
Lynch-1	Linear force free	0.7	48.1	0.45
Lynch-2	Linear force free	-4	63.1	0.63
Lynch-3	Linear force free	-18.7	73.4	0.57
Lynch-4	Linear force free	-33.8	171.0	0.91
Rees	Linear force free	-26.8	6.3	0.4

4 Summary and Discussion

In this study we have applied 5 FRF techniques to 2 time series derived from a global MHD simulation of an interplanetary CME. The results have, in general, reinforced the usefulness of such approaches for analyzing magnetic clouds in the solar wind. However, they have also raised some caveats:

1. As noted by Lepping et al. (1990), techniques relying on minimum variance to identify the orientation of the cloud axis limit the technique to those events

3.7 General Comparison of the Results

Each team was asked to perform their "typical" analysis on the two cases, resulting in a variety of fitted parameters, error estimates, and auxiliary information. For our initial study, we have chosen to limit the comparison to the 4 parameters that were computed by every model. These are: (1) the sign of the cloud helicity; (2) the latitude of the cloud axis (Λ); (3) the azimuth of the cloud axis (φ); and (4) the impact parameter (P).

3.7.1 Cloud Helicity

Every team correctly identified the sign of the helicity as being left-handed (-1) for case A. Moreover, with the exception of the Lynch team, they also inferred the same handedness for case B. This is not particularly surprising for case A, where the fits were generally very good; however, it demonstrates that even when the fits are poor (i.e., case B), helicity is apparently a robust and reliably-inferred parameter.

3.7.2 Latitude and Azimuth of the Cloud Axis

The cloud axis orientations for cases A and B are summarized in Tables 1 and 2, respectively. The Lepping and Lynch teams performed multiple fits to the events by varying the location of the boundaries, and all are included for completeness. For case A, most fits are within $10° - 15°$ of the correct MHD result of $\Lambda = 0°$ and $\varphi = -90°$. Note also that even when larger discrepancies occur in latitude, the azimuthal orientation remains within 15°. In contrast, the case B results stray substantially. The latitudinal orientations show less scatter; however, the azimuthal orientations are, for some events, orthogonal to the MHD solution.

3.7.3 Impact Parameter

The final columns in Tables 1 and 2 provide the calculated impact parameters. For case A, they are generally ≤ 0.1. Given the kinematic and dynamic evolution of the CME during its passage to 1 AU, the effective location of the axis of the cloud cannot be precisely determined, and any value ≤ 0.1 would appear to be consistent with the MHD solution. The impact parameters calculated for case B show more scatter, but generally fall into the range of $0.4 - 0.7$. These are systematically lower than the result deduced from the global picture shown in Figure 1 ($P = 0.7$).

for which the spacecraft passes relatively close to the axis.

2. While identifying boundaries for simple events (i.e., case A) is straightforward, for more complex structures, it becomes a significant challenge. In fact, if the field vectors and magnitude do not conform to the standard variations (i.e., rotation and field enhancement), the results of the fit must be seriously questioned. The elliptical cross section model does not avoid this pitfall as it is capable of fitting to almost any profile. Only the GSR technique, for which the boundaries are a model output, can in principle circumvent this. However, this remains to be tested. It may be that a combined model using the GSR technique to locate the boundaries of the cloud and the elliptical cross section model to compute the cloud parameters, for example, may provide the optimal solution.

3. The global picture of the flux rope implied by the GSR technique and the ellipticity inferred from the elliptical cross section model did not capture the true distortion of the flux rope. The aspect ratio, defined as the flux ropes latitudinal extent relative to its radial extent, can be inferred from Figure 1 to be approximately 5-6 as it approaches 1 AU. We have shown previously (Riley and Crooker, 2004) that this is a predominantly kinematic, and not a dynamic effect. It is likely that the GSR's magnetostatic assumption contributes to its underestimate of the large aspect ratio of the event.

We have shown (Riley and Crooker, 2004) that the fundamental cross section of flux ropes in the solar wind is neither circular nor elliptical, but rather a convex-outward, "pancake" shape. We believe that FRF techniques would benefit greatly by incorporating this kinematic distortion. One way to accomplish this would be to include an "aspect ratio" free parameter. However, unlike the elliptical cross section model by Hidalgo et al. (2002), it should be based on an arc sweeping perpendicular to the Earth-Sun line through the flux rope.

In spite of these limitations, FRF models: (1) are easy to apply to in situ measurements; and (2) provide the only way to infer the cloud's orientation, sign of the helicity, and radial dimension. Thus they are likely to remain an important tool for analyzing magnetic clouds for the foreseeable future. Care, however, should be taken when interpreting the results. Global inferences must be viewed cautiously, even when the fit to the observations is good (e.g., Figure 4, Case A). When the fits to the data are poor, even the basic fit parameters should be questioned.

This study represents our first attempt to assess the accuracy and validity of FRF techniques. Our results suggest a number of avenues to pursue in the future. For example, fitting to a sequence of MHD time series that are increasingly further from the axis (with prior knowledge of the flux rope boundaries)

would allow us to quantify errors introduced by larger impact parameters. Also, generating - and fitting to - MHD solutions of flux ropes with a range of speeds would allow us to assess the role that interplanetary dynamics plays on the quality of the fits. Finally, flying through different locations of a localized 3-D eruption would allow us to investigate spatial effects on the fits.

Acknowledgments PR gratefully acknowledges the support of the National Aeronautics and Space Administration (LWS Program) and the National Science Foundation (SHINE Program and the Center for Integrated Space Weather Modeling) in undertaking this study. QU was supported by a CIT subcontract PC251439 under NASA grant NAG5-6912 for the ACE project.

References

Burlaga, L. F., 1988. Magnetic clouds and force free-fields with constant alpha. J. Geophys. Res. 93, 7217.

Burlaga, L. F., Sittler, E. C. J., Mariani, F., Schwenn, R., 1981. Magnetic loop behind an interplanetary shock - voyager, helios, and imp-8 observations. J. Geophys. Res. 86, 6673.

Chen, J., 1996. Theory of prominence eruption and propagation: Interplanetary consequences. J. Geophys. Res. 101 (A12), 27499.

Goldstein, H., 1983. On the field configuration in magnetic clouds, in solar wind five. In: Neugebauer, M. (Ed.), NASA Conf. Publ. Vol. CP-2280. NASA Conf. Publ., p. 731.

Gosling, J. T., 1990. Coronal mass ejections and magnetic flux ropes in interplanetary space. IN: Physics of magnetic flux ropes 58, 343.

Hau, L. N., Sonnerup, B. U. O., 1999. Two-dimensional coherent structures in the magnetopause: Recovery of static equilibria from single-spacecraft data. J. Geophys. Res. 104, 6899.

Hidalgo, M. A., Cid, C., Vinas, A. F., Sequeiros, J., 2002. A non-force-free approach to the topology of magnetic clouds in the solar wind. J. Geophys. Res. 107 (A1), DOI 10.1029/2001JA900100.

Hidalgo, ., 2003. A study of the expansion and distortion of the cross section of magnetic clouds in the interplanetary medium. J. Geophys. Res. 108 (A8), DOI 10.1029/2002JA009818.

Hu, Q., Smith, C. W., Ness, N. F., Skoug, R. M., 2003. Double flux-rope magnetic cloud in the solar wind at 1 au. Geophys. Res. Lett. 30 (7), 38.

Hu, Q., Sonnerup, B., 2002. Reconstruction of magnetic clouds in the solar wind: Orientations and configurations. J. Geophys. Res. 107 (A7), DOI 10.1029/2001JA000293.

Hu, Q., Sonnerup, B. U. O., 2001. Reconstruction of magnetic flux ropes in the solar wind. Geophys. Res. Lett. 28 (3), 467.

Hu, Q., Sonnerup, B. U. ., 2000. Magnetopause transects from two spacecraft: A comparison. Geophys. Res. Lett. 27 (10), 1443.

Hundhausen, A. J., 1987. The origin and propagation of coronal mass ejections. In: Pizzo, V. J., Holzer, T. E., Sime, D. G. (Eds.), in the Sixth International Solar Wind Conference, Proceedings of the conference held 23-28 August, 1987. Vol. 2. at YMCA Technical Note Natl. Cent. for Atmos. Res., Boulder, Colo., p. 181, tech. Note TN-306.

Lepping, R. P., Berdichevsky, D. B., Ferguson, T. J., Oct. 2003. Estimated errors in magnetic cloud model fit parameters with force-free cylindrically symmetric assumptions. J. Geophys. Res., 1–1.

Lepping, R. P., Jones, J. A., Burlaga, L. F., 1990. Magnetic field structure of interplanetary magnetic clouds at 1 au. J. Geophys. Res. 95, 11957.

Lundquist, S., 1950. Magnetostatic fields. Ark. Fys. 2, 361.

Marubashi, K., 1997. Interplanetary magnetic flux ropes and solar filaments, in coronal mass ejections. In: Crooker, N. U., Joselyn, J. A., Feynman, J. (Eds.), Coronal Mass Ejections (Geophys. Monogr.). Vol. 99. AGU, Washington, DC, p. 147.

Mikić, Z., Linker, J. A., 1994. Disruption of coronal magnetic field arcades. Astrophys. J. 430, 898.

Mulligan, T., Russell, C. T., Anderson, B. J., Acuna, M. H., 2001. Multiple spacecraft flux rope modeling of the bastille day magnetic cloud. Geophys. Res. Lett. 29 (23), 4417.

Odstrcil, D., Linker, J. A., Lionello, R., Mikić, Z., Riley, P., Pizzo, V. J., Luhmann, J. G., 2002. Merging of coronal and heliospheric numerical 2-d mhd models. J. Geophys. Res. 107 (A12), DOI 10.1029/2002JA009334.

Odstrcil, D., Pizzo, V. J., 1999. Three-dimensional propagation of coronal mass ejections in a structured solar wind flow, 1, cme launched within the streamer belt. J. Geophys. Res. 104 (A1), 483.

Odstrcil, D., Riley, P., Linker, J. A., Lionello, R., Mikic, Z., Pizzo, V. J., ???? 3-D simulations of ICMEs by coupled coronal and heliospheric models. In: ESA SP-535: Solar Variability as an Input to the Earth's Environment. pp. 541–+.

Osherovich, V., Farrugia, C., Burlaga, L., 1993. Dynamics of aging magnetic clouds. Adv. Space Res. 13 (6), 57.

Riley, P., Crooker, N. U., 2004. Kinematic treatment of cme evolution in the solar wind. Accepted for publication in Astrophysical Journal.

Riley, P., Linker, J. A., Mikić, Z., 2002a. Modeling the heliospheric current sheet: Solar cycle variations. J. Geophys. Res. 107 (A7), DOI 10.1029/2001JA000299.

Riley, P., Linker, J. A., Mikić, Z., Odstrcil, D., Pizzo, V. J., Webb, D. F., 2002b. Evidence of posteruption reconnection associated with coronal mass ejections in the solar wind. Astrophys. J. 578 (2), 972.

Riley, P., Linker, J. A., Mikić, Z., Odstrcil, D., Zurbuchen, T. H., Lario, D. A., Lepping, R. P., 2003. Using an mhd simulation to interpret the global context of a coronal mass ejection observed by two spacecraft. Accepted for

publication in J. Geophys. Res. 108 (A7), DOI 10.1029/2002JA009760.
Sonnerup, B. U. O., Cahill, L. J., J., 1967. Magnetopause structure and attitude from explorer 12 observations. J. Geophys. Res. 72, 171.
Sonnerup, B. U. O., Guo, M., 1996. Magnetopause transects. Geophys. Res. Lett. 23, 3679.
Vandas, M., Romashets, E. P., Feb. 2003. A force-free field with constant alpha in an oblate cylinder: A generalization of the Lundquist solution. Astron. Astrophys. 398, 801–807.
Webb, D. F., Howard, R. A., 1994. The solar cycle variation of coronal mass ejections and the solar wind mass flux. J. Geophys. Res. 99 (A3), 4201.